J. Fluid Mech. (2001), *vol.* 432, *pp.* 69–90. Printed in the United Kingdom

Acoustic receptivity and evolution of two-dimensional and oblique disturbances in a Blasius boundary layer

By RUDOLPH A. KING[1] AND KENNETH S. BREUER[2]

[1]NASA Langley Research Center, Hampton, VA 23681, USA

[2]Division of Engineering, Brown University, Providence, RI 02912, USA

(Received 21 April 2000 and in revised form 2 October 2000)

An experimental investigation was conducted to examine acoustic receptivity and subsequent boundary-layer instability evolution for a Blasius boundary layer formed on a flat plate in the presence of two-dimensional and oblique (three-dimensional) surface waviness. The effect of the non-localized surface roughness geometry and acoustic wave amplitude on the receptivity process was explored. The surface roughness had a well-defined wavenumber spectrum with fundamental wavenumber k_w. A planar downstream-travelling acoustic wave was created to temporally excite the flow near the resonance frequency of an unstable eigenmode corresponding to $k_{ts} = k_w$. The range of acoustic forcing levels, ϵ, and roughness heights, Δh, examined resulted in a linear dependence of receptivity coefficients; however, the larger values of the forcing combination $\epsilon\Delta h$ resulted in subsequent nonlinear development of the Tollmien–Schlichting (T–S) wave. This study provides the first experimental evidence of a marked increase in the receptivity coefficient with increasing obliqueness of the surface waviness in excellent agreement with theory. Detuning of the two-dimensional and oblique disturbances was investigated by varying the streamwise wall-roughness wavenumber α_w and measuring the T–S response. For the configuration where laminar-to-turbulent breakdown occurred, the breakdown process was found to be dominated by energy at the fundamental and harmonic frequencies, indicative of K-type breakdown.

1. Introduction

The transition of a boundary layer from a laminar to a turbulent state plays an important role in many fluid mechanics problems since it ultimately affects basic quantities such as heat transfer and skin friction. This transition process is affected by many factors such as free-stream (turbulence and/or acoustical) and surface disturbances. The process by which these disturbances are internalized to generate boundary-layer instability waves is referred to as *receptivity* (Morkovin 1969). The most widely used transition prediction tool is currently the e^N method, which is a semi-empirical method based on linear amplification (not disturbance amplitudes) of unstable modes. This approach does not include any physics regarding the role of the external disturbance environment on the boundary-layer instability development. Improved transition prediction tools based on an amplitude approach need to incorporate physics relating the effects of the environment on the transition process. This approach needs, as an input, information about the initial boundary-layer disturbance amplitude, and this need is met by a better understanding of the receptivity process.

Consequently, receptivity plays a crucial role in any transition prediction tool that utilizes an amplitude-based approach. Because of the significant wavelength mismatch between the long-wavelength external disturbances and the much shorter-wavelength Tollmien–Schlichting (T–S) waves, a length-scale conversion must take place to facilitate the energy transfer. It has been shown theoretically (see for example Goldstein 1983, 1985; Goldstein, Sockol & Sanz 1983; Zavol'skii, Reutov & Rybushkina 1984; Ruban 1985) that wavelength-reduction mechanisms can range from direct scattering associated with abrupt changes in surface conditions to the gradual wavelength reduction due to viscous boundary-layer growth.

Two general classes of receptivity regions were recognized by Goldstein: (I) the leading-edge regions where the boundary layer is thin and growing rapidly and (II) regions further downstream where the boundary layer is forced to make a rapid adjustment. A common feature of both receptivity regions is the importance of non-parallel effects and is manifested via the disturbance motion being governed by the unsteady boundary-layer equations. Class II can be further subdivided into *localized* and *non-localized* receptivity. Localized receptivity results from an interaction between the free-stream disturbances and steady localized disturbance generated by a surface inhomogeneity (e.g. humps, gaps, or suction/blowing slots). Non-localized receptivity stems from an interaction in boundary-layer flow with unsteady free-stream disturbances and the steady disturbance created over surfaces with extended regions of short-scale variations (e.g. waviness, distributed roughness, uneven suction, etc.).

Choudhari (1993) investigated the extent of synchronization between the surface waviness and neutral instability motion, where for perfect resonance at Branch I (lower branch) $\alpha_w = \alpha_{ts,I}$. Here α_w and α_{ts} denote the wall wavenumber and instability wavenumber, respectively and the subscript I refers to conditions at Branch I. He shows that the resonance region corresponds to a spatial extent of $\Delta x = O(x_I R_I^{-3/8})$ where x denotes streamwise distance and $R(= Re_x^{1/2})$ Reynolds number. This implies that a synchronized surface waviness will lead to instability amplitudes which are larger than those produced by an isolated surface roughness by a factor of $O(R_I^{3/8})$. Choudhari's simple analytical result helped to explain some earlier results computed by Crouch (1991, 1992) where he found significantly larger values for non-localized receptivity than localized receptivity. Crouch & Bertolotti (1992) have shown non-localized receptivity amplitudes to be large over a wide range of surface wavenumber. They also show an increase of receptivity with surface roughness three-dimensionality.

Numerous acoustic receptivity experiments have been performed with two-dimensional surface roughness (e.g. Aizin & Polyakov 1979; Saric, Hoos & Kohama 1990; Saric, Hoos & Radeztsky 1991; Wiegel & Wlezien 1993; Zhou, Liu & Blackwelder 1994; Kosorygin, Radeztsky & Saric 1995; Kobayashi *et al.* 1995; Kobayashi, Fukunishi & Kato 1996; Breuer *et al.* 1996; Saric & White 1998). All of these studies were conducted for localized two-dimensional receptivity except for that by Wiegel & Wlezien (1993) where they considered non-localized receptivity. The experiment of Zhou *et al.* (1994) also considered receptivity of an oblique surface roughness. That study was conducted for localized oblique receptivity where a single strip of tape was inclined at angles up to $\psi_w = 45°$. They inferred from their measurements at a fixed streamwise location that receptivity was reduced with increased oblique angle. They did not consider the reduced linear growth rates associated with increased obliqueness.

The objectives of this research were to further understand the acoustic receptivity process for flow over wavy surfaces and to correlate theoretical results with experimental results. The approach taken was to experimentally investigate acoustic

receptivity in the presence of surface waviness and the subsequent boundary-layer disturbance evolution. Previous experimental acoustic receptivity data (Wiegel & Wlezien 1993) in the presence of two-dimensional surface waviness demonstrated excellent agreement with theoretical receptivity coefficients (Crouch 1992; Choudhari 1993). Previous experimental data, in the presence of oblique surface waviness, do not exist and inference made from previous experimental results (Zhou *et al.* 1994) for a localized oblique roughness strip contradict theoretical findings. The current experimental study with two-dimensional waviness was conducted to (i) validate the current approach with respect to previous experimental and theoretical results and (ii) extend the measurements into regions of nonlinear T–S wave development. The measurements were then extended to include, for the first time, experimental data obtained with oblique surface waviness for comparison with theory (Crouch & Bertolotti 1992). Receptivity/stability experiments are very sensitive to the state of the mean flow and environmental disturbances. As a result, extreme care was taken to document the flow and environmental conditions to avoid ambiguous results as discussed by Nishioka & Morkovin (1986) and Saric (1994).

2. Experimental details

2.1. *Facility and model*

The experiment was conducted in the 2 ft. by 3 ft. Low-Speed Wind Tunnel located at NASA Langley Research Center. The tunnel is a closed-loop type with a 10 : 1 contraction ratio. The test section is 0.91 m wide by 0.61 m high by 6.1 m long. The turbulence-reduction devices upstream of the contraction consist of a honeycomb followed by four stainless-steel screens. Speeds of approximately 45 m s^{-1} are attainable in the test section with measured turbulence intensities, u/U_∞, of approximately 0.1% in the range of $0.1 < f < 400$ Hz. The test-section floor and ceiling are adjustable to achieve a desired streamwise pressure gradient. Two motorized traverse stages, one with streamwise travel of 2.1 m and the other with vertical travel of 150 mm, are located just above the test section ceiling. The quoted accuracies of the streamwise (x) and vertical (y) traverse stages are $\pm 166\,\mu$m m^{-1} and $\pm 30\,\mu$m m^{-1}, respectively. A 3.8 cm streamwise slot (covered with rectangular wool felt strips to minimize air inflow/outflow) along the centreline of the tunnel ceiling is provided to accommodate a probe support for two-dimensional traverse motion.

The model tested was a 12.7 mm thick flat aluminium jig plate with a 24 : 1 elliptical leading edge. A sketch of the model is shown in figure 1. Because of the potential sensitivity of the receptivity/stability characteristics to surface roughness, the upper surface (measurement side) of the model was polished to a 0.2 μm root-mean-square (r.m.s.) surface finish. The boundary layer on the lower surface of the model was tripped using sandpaper grit to establish turbulent flow on that surface. The plate was equipped with a rectangular hole located 24.6 cm from the model leading edge for the installation/removal of plate inserts. Five inserts were available for the test. One was used as the baseline (smooth sample) and four were used to mount various samples of receptivity sites. Further details of the experimental setup are given by King (2000).

2.2. *Surface roughness and acoustic excitation*

Receptivity was facilitated by the use of surface waviness of height Δh and free-stream acoustic excitation with amplitude u_{ac}. In previous experiments, receptivity sites were usually created by applying tape or some other adhesive material to the surface of

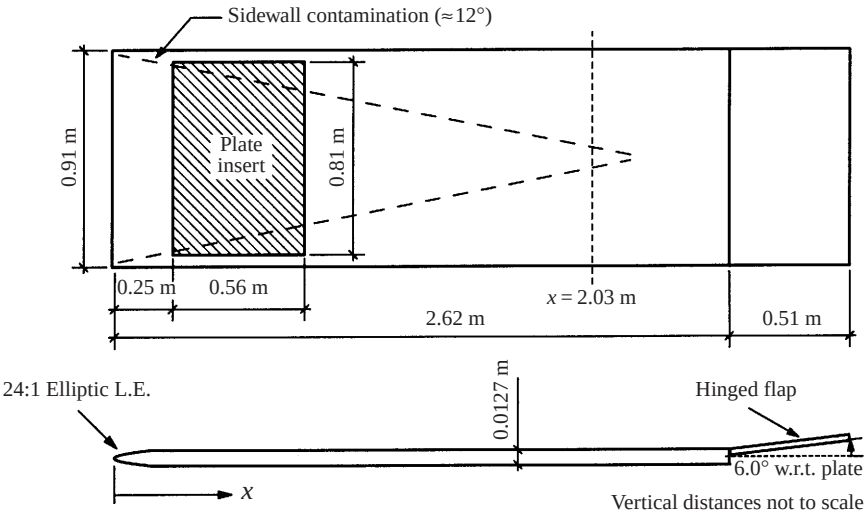

FIGURE 1. Top and side views of the flat-plate model. The shaded region represents the location of the insert.

the model. For the case of non-localized receptivity, this is a very tedious process (e.g. slight misalignment – angular and/or spatial – of the tape, Δh non-uniformities, etc.). An alternative approach for generating the surface roughness was considered, which involved the use of copper-plated circuit boards. The roughness patterns were generated using a photolithographic process where a high degree of spatial accuracy was maintained. In this process a pattern was transferred from a photomask to a material layer to produce a two-layer pattern with the roughness height Δh being equal to the copper plating thickness. The two types of patterns considered are represented in figure 2 (the shaded areas represent copper and flow is from top to bottom). The first was a two-dimensional waviness pattern ($\psi_w = 0$) with the wavenumber vector parallel to the stream direction. The second was an oblique waviness pattern where the wavenumber vector makes an angle ψ_w with the stream direction. Highly localized disturbances are possible for the oblique patterns as a result of the sharp steps formed by the copper strips at the leading and trailing edges of the samples. To mitigate this effect, the copper strips were feathered down to the substrate material 6.4 mm from both the leading and trailing edges of the samples. The roughness patterns considered are presented in table 1.

The tunnel was equipped with an array of five 203.3 mm diameter woofers (four flush mounted on the upstream wall and the other on the downstream wall) for acoustic excitation. The speakers were located as described to minimize unwanted flow disturbances in the tunnel. The backplanes of the speakers were sealed in boxes with bleed holes to equilibrate the mean pressures on both sides of the diaphragms. The source of the controlled acoustic field was generated by using a dual-channel universal source and amplified with a stereo power amplifier. One channel of the source was used to drive the four upstream speakers and the second channel for the one downstream speaker. The ability to control the absolute amplitude and relative phase of the two channels made it possible to generate the required acoustic field in the test section.

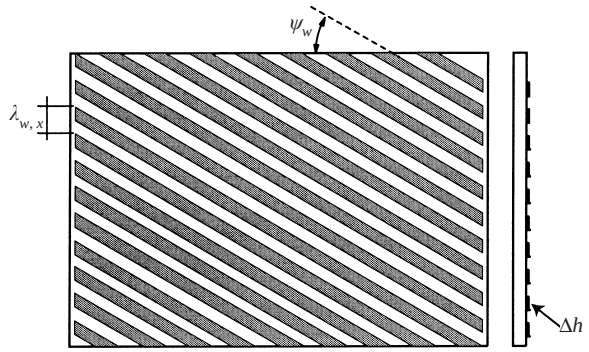

FIGURE 2. Top and side views of the receptivity sites investigated: $\psi_w = 0$ for two-dimensional and $\psi_w \neq 0$ for oblique roughness. Flow is from top to bottom.

Sample	Δh (μm)	$\lambda_{w,x}$ (mm)	ψ_w (deg.)
1	17.8	50.25	0
2	35.6	50.25	0
3	71.1	50.25	0
4	35.6	58.88	0
5	35.6	53.34	0
6	35.6	50.80	0
7	35.6	49.53	0
8	35.6	48.26	0
9	35.6	45.72	0
10	35.6	50.75	15
11	35.6	52.36	30
12	35.6	55.48	45
13	35.6	56.67	32
14	35.6	54.50	31
15	35.6	50.27	29
16	35.6	48.22	28

TABLE 1. Table of roughness samples tested, where $\lambda_{w,x}$ is the streamwise wavelength.

2.3. *Data reduction*

A single hot-wire probe was used to measure the streamwise velocity component, which represents the bulk of the experimental data. A constant-temperature anemometer was configured to use a 1:20 bridge with a wire resistive overheat ratio of 1.8. A fourth-order polynomial curve fit was found to work well for the hot-wire calibration, velocity versus output voltage. Broadband and phase-locked velocity fluctuations were acquired using a typical sampling rate of 1 kHz. The mean tunnel properties (pressures, temperature and relative humidity) were measured and recorded at each data point. Estimated uncertainties of measured mean velocity, U, are in the range $\pm 1.4\%$ for $U_{max} \approx 11.1\,\mathrm{m\,s^{-1}}$ to $\pm 9.0\%$ for $U_{min} \approx 1\,\mathrm{m\,s^{-1}}$. Uncertainties of r.m.s. fluctuating velocity, u, and Reynolds number, Re_l ($= U_\infty l/\nu$), are $\pm 4.7\%$ and $\pm 4.0\%$, respectively. Details of the error analysis are given by King (2000).

Because of the type of acoustic excitation (i.e. continuous wave), the measured r.m.s. narrow-band velocities $u_t \exp(\mathrm{i}\phi_t)$ included the Stokes wave, the T–S response, and any other extraneous response (e.g. probe vibration) all at the same excitation frequency f_o. A Stokes wave is present whenever an oscillating velocity disturbance

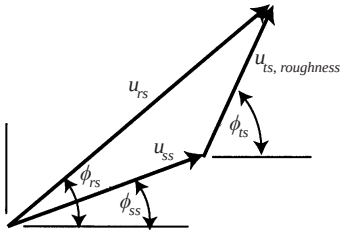

FIGURE 3. Graphical representation of the decomposition method used for wall-normal surveys.

exists in the free stream. Wlezin, Parekh & Island (1990) and Wlezien (1994) found that consistent estimates of the T–S modes are achieved when the Stokes wave is directly estimated from the measured profiles. The various decomposition approaches exploit the fact that a large mismatch in length scales exists between the Stokes and T–S waves, a 95 : 1 ratio for this study. One such approach is to make short streamwise surveys that cover approximately one T–S wavelength, λ_{ts}, at a fixed height in the boundary layer (see Wlezien 1994; Saric *et al.* 1995). Over one λ_{ts}, the phase of the Stokes wave (and for that matter any probe vibration) is for all practical purposes constant. The measured response can then be plotted on the polar complex plane. Since the T–S amplitude does not vary significantly over one λ_{ts}, the centroids (Stokes wave + vibration) and the average radii (T–S amplitudes) of the off-centred spirals can be computed. The T–S wave measured here includes receptivity contributions from all possible sources, the leading edge and receptivity sites. Such surveys were obtained at wall-normal locations of lower maxima of the T–S mode shapes. Because the T–S wave is a travelling wave (i.e. linear phase ϕ_{ts} w.r.t. x), linear regression was employed to compute the streamwise T–S wavenumber, $\alpha_{ts} = |\mathrm{d}\phi_{ts}/\mathrm{d}x|$, which was used to obtain wave kinematic results (e.g. streamwise wavelength $\lambda_{ts,x}$ $(= 2\pi/\alpha_{ts})$, phase speed c_{ph} $(= 2\pi f_o/\alpha_{ts})$, etc.).

Most of the disturbance measurements were acquired by making wall-normal surveys, complete and partial boundary-layer profiles, at selected x locations. The approach taken here to extract the T–S wave component is a slight variation of earlier methods (e.g. Wlezien 1994; Saric *et al.* 1995). Two sets of wall-normal disturbance profiles were obtained at the same x locations and with the same acoustic forcing levels. One set was taken with the smooth surface (denoted with *ss* subscripts) and the second with a rough surface (denoted by subscript *rs*). The disturbance measurements obtained on the smooth surface include components of the Stokes wave, T–S wave due to leading-edge receptivity, and extraneous disturbances. The disturbances acquired with receptivity sites include the same components measured on the smooth surface in addition to the T–S wave component due to the controlled roughness. This is shown graphically in figure 3. The T–S wave component due to roughness was obtained using

$$u_{ts}\mathrm{e}^{\mathrm{i}\phi_{ts}} = u_{rs}\mathrm{e}^{\mathrm{i}\phi_{rs}} - u_{ss}\mathrm{e}^{\mathrm{i}\phi_{ss}}. \tag{2.1}$$

Here the T–S component includes receptivity due to acoustic scattering at the roughness sites of (i) the free-stream acoustic field and (ii) the leading-edge-generated T–S wave. The receptivity due to (ii) was assumed negligibly small. This was supported by leading-edge receptivity measurements in the present study and a previous experiment by Wlezien *et al.* (1990) for a 24 : 1 elliptic leading edge, both of which indicated small T–S responses.

Linear stability results presented here were computed using a computer code by Malik (1992) that incorporates quasi-parallel spatial stability theory. These results were

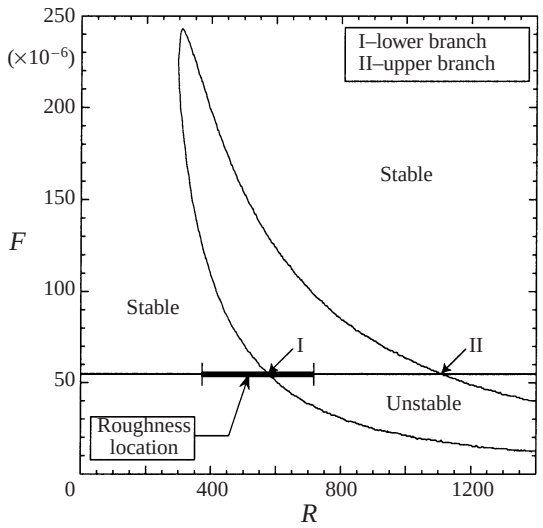

FIGURE 4. Neutral stability curve for a Blasius boundary layer with two-dimensional disturbances.

used to facilitate the computation of the receptivity coefficients, C $(= u_{ts,I}/u_{ac})$, referenced to the Branch I location. Here $u_{ts,I}$ denotes the maximum r.m.s. T–S amplitude at Branch I and u_{ac} the r.m.s. free-stream acoustic velocity fluctuation. Measurements of u_{ts} were made downstream of Branch I to take advantage of the linear amplification region for improved signal-to-noise ratios. The values of $u_{ts,I}$ were obtained by applying linear stability theory (LST) to the measured values of u_{ts} such that

$$C = \frac{u_{ts}\mathrm{e}^{-N}}{u_{ac}} \tag{2.2}$$

where

$$N\left(= \int_{x_I}^{x} -\alpha_i(x;f)\mathrm{d}x\right)$$

is the amplification factor and α_i is the spatial amplification rate obtained from LST.

2.4. *Experimental approach*

This experiment was conducted with a nominal free-stream velocity of $U_\infty = 11.1\,\mathrm{m\,s^{-1}}$ and temperature of 21 °C. A nominally zero-streamwise-pressure-gradient boundary layer was obtained for flow over a flat plate (Blasius flow). A planar downstream-travelling acoustic wave was used to temporally excite the flow with frequency f_o. A simple approach was employed to generate the wave train by conducting two streamwise surveys in the free-stream above the model, each at the same spatial coordinates. One survey was taken with only the upstream set of speakers activated and the second survey with only the downstream speaker energized. Applying the method of superposition, the combined wave field with both sets of speakers active was simulated. A scale factor and phase shift were selected to give the desired response, namely, a constant r.m.s. amplitude distribution.

The dimensionless frequency of the T–S wave for all cases was $F = 55 \times 10^{-6} (= 2\pi f \nu / U_\infty^2)$, which translates to physical acoustic forcing frequency of $f_o = 71\,\mathrm{Hz}$. Figure 4 shows a plot of a neutral stability curve for a Blasius boundary layer with two-dimensional disturbances. A line representing the experimental frequency along with the roughness location and extent ($\Delta x = 0.56\,\mathrm{m}$) is shown in the figure.

	Δh_1	$\Delta h_2 = 2\Delta h_1$	$\Delta h_3 = 4\Delta h_1$
ϵ_1	$\epsilon_1 \Delta h_1$	$2\epsilon_1 \Delta h_1$	$4\epsilon_1 \Delta h_1$
$\epsilon_2 \doteq 2\epsilon_1$	$2\epsilon_1 \Delta h_1$	$4\epsilon_1 \Delta h_1$	$8\epsilon_1 \Delta h_1$
$\epsilon_3 \doteq 4\epsilon_1$	$4\epsilon_1 \Delta h_1$	$8\epsilon_1 \Delta h_1$	$16\epsilon_1 \Delta h_1$

TABLE 2. Roughness heights and acoustic forcing levels examined: $\Delta h_1 = 17.8\,\mu\text{m}$, $\epsilon_1 = 7.6 \times 10^{-5}$ ($SPL = 84.8$).

Note that the location of the surface waviness was selected such that its midpoint was near the location of Branch I to maximize the receptivity. The wavenumber of the surface roughness, k_w ($= [\alpha_w^2 + \beta_w^2]^{1/2}$), was selected such that it matched the T–S wavenumber, k_{ts}, at Branch I to provide a near-resonance condition. Three roughness heights, Δh, and three acoustic forcing levels, ϵ ($= u_{ac}/U_\infty$), were examined for the two-dimensional waviness. The matrix configuration used to combine Δh and ϵ are given in table 2. The smallest roughness height and acoustic forcing level examined are $\Delta h_1 = 17.8\,\mu\text{m}$ and $\epsilon_1 = 7.6 \times 10^{-5}$ (i.e. $SPL = 84.8$ at f_o), respectively. Detuning was examined for the two-dimensional and oblique roughness patterns. This was achieved by maintaining the same forcing frequency, f_o, and varying the streamwise wall roughness wavenumber, α_w, while the spanwise wavenumber, β_w, remained unchanged.

3. Results and discussion

3.1. *Base flow measurements*

3.1.1. *Mean flow*

Normalized streamwise velocity measurements just outside the boundary layer, $y \approx 25.4\,\text{mm}$, revealed a pressure recovery region near the leading edge of the model with deviations of less than 0.25 % of U_∞ from the Branch I location to the end of the survey region ($0.5 < x < 2.03\,\text{m}$). The velocities along the plate insert location for roughness placement ($24.6 < x < 80.8\,\text{cm}$) were all within 1% of U_∞. For the properly configured model, the boundary layer developed into a nominally zero-pressure-gradient boundary layer downstream of the recovery region. For proper comparisons with theory, a virtual origin was defined and streamwise locations referenced to this origin are denoted by x_v. The virtual origin was computed by first acquiring detailed boundary-layer velocity profiles on the smooth (baseline) model every 254 mm starting at $x = 508\,\text{mm}$. A linear-regression curve fit was applied to the square of the measured displacement thickness (δ^*) versus x. The curve fit was used to extrapolate upstream to $\delta^* = 0$ and the corresponding x value was used as the virtual origin, $x = 65.8\,\text{mm}$.

A more stringent characterization of the flow was to compute the shape factor H for each profile. The values of the experimental shape factors were $H = 2.60 \pm 1.5\%$ in excellent agreement with the theoretical Blasius value of $H = 2.59$. A plot of the measured normalized velocity profiles and the theoretical Blasius profile versus the normalized wall-normal coordinate η ($= [y/x_v]Re_{x_v}^{1/2}$) is presented in figure 5. Excellent agreement between the profiles is evident. The two-dimensionality of the mean flow outside the sidewall contamination region (see figure 1) was validated by obtaining boundary-layer measurements at various spanwise locations.

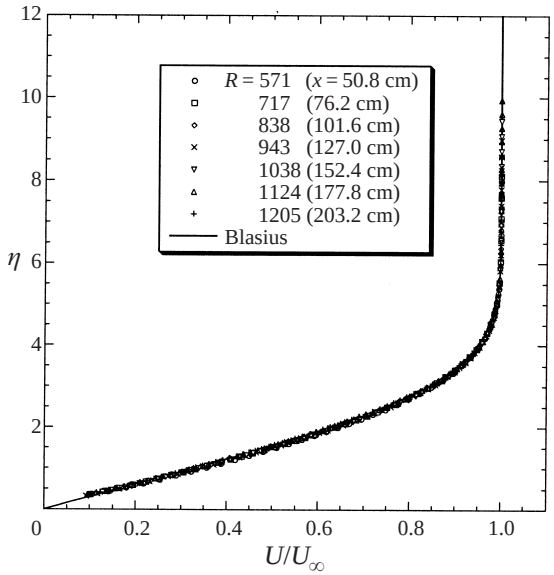

FIGURE 5. Normalized velocity profiles at selected streamwise locations.

3.1.2. *Free-stream characteristics*

Free-stream turbulent intensity measurements $(u/U)_\infty$, where u is the broadband r.m.s. value of velocity fluctuations ($0.1 < f < 400$ Hz), were obtained using a single hot-wire probe. Values of $(u/U)_\infty \approx 0.1\%$ were measured over the entire streamwise survey region. More important than the magnitude of $(u/U)_\infty$, the power spectral density of the fluctuating velocity, PSD_u, provided relevant information on the frequency content of the disturbance environment. Measured PSD_u values indicate a $-5/3$ power law ($PSD_u \propto f^{-5/3}$), supporting the hypothesis that the free-stream disturbances were composed predominantly of decaying turbulence. Most of the free-stream energy was contained at very low frequencies, below 1 Hz. More than 90% of the broadband energy was contained between 0.1 Hz and 1 Hz illustrating the importance of specifying frequency bandwidths when quoting turbulent levels. Limited dynamic pressure measurements were obtained from four pressure transducers flush mounted on the test section sidewalls (details given by King 2000). Correlations of the dynamic pressure signals confirm the absence of coherent disturbances in the free-stream environment near the designed forcing frequency, f_o, of the experiment that can distort the interpretation of the results.

As a final flow-quality check, the transition Reynolds number, Re_{tr}, was measured on the smooth plate. This was done by placing the hot-wire probe at a fixed location in the boundary layer and slowly sweeping through the tunnel speed range. An average value of $Re_{tr} = 3.2 \times 10^6$ was measured, indicating low free-stream turbulent levels and a smooth model surface (for comparison, refer to data of Re_{tr} versus free-stream turbulence cited in White (1974, pp. 433–436). For a configuration with two-dimensional waviness ($\Delta h = 71.1\,\mu$m) and $\epsilon = 0$, a 25% reduction in Re_{tr} was observed.

3.1.3. *Acoustic-field characterization*

Measurements of the controlled free-stream acoustic field are shown in figure 6 in the form of (*a*) amplitude and (*b*) phase streamwise distributions. Data with only the

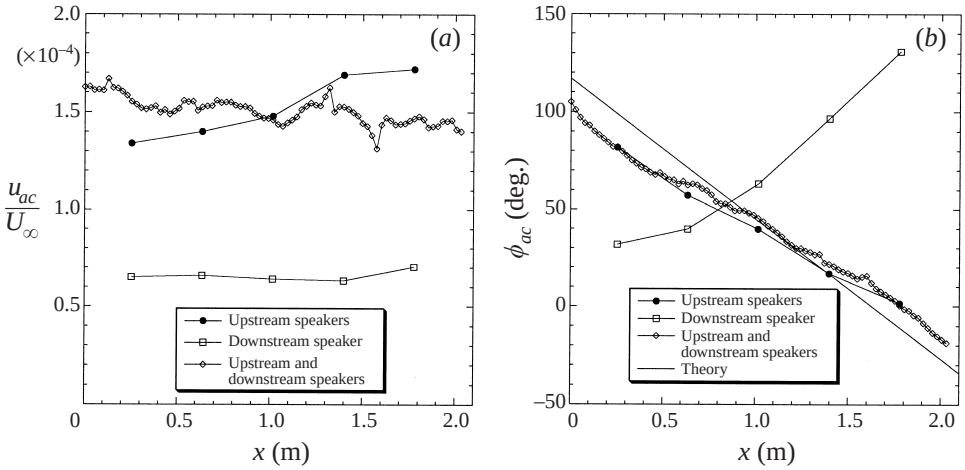

FIGURE 6. Measured free-stream acoustic field generated in the test section above the model surface: (*a*) amplitude and (*b*) phase streamwise distributions.

ψ_{ts} (deg.)	R_I	$\lambda_{ts,I,x}$ (mm)
0	585	50.2
15	583	50.8
30	578	52.4
45	574	55.5

TABLE 3. Tabulated data of Reynolds numbers and streamwise T–S wavelength at Branch I for disturbance wave angle ψ_{ts} obtained from LST. Note that $R \approx 85.92x_v^{1/2}$ where x_v is in centimeters.

upstream speakers and only the downstream speaker activated are also presented for completeness in the figure. In the vicinity of the insert region ($24.6 < x < 80.8$ cm), the variation of the acoustic amplitude was small. The phase distribution in figure 6(*b*) indicates a predominantly downstream-travelling wave. Values of the acoustic r.m.s. amplitudes, u_{ac}, used for normalization in subsequent sections are the average values measured over the plate insert. Streamwise measurements taken at various wall-normal and spanwise locations verified the planar structure of the acoustic field.

3.2. *Receptivity measurements*

3.2.1. *Effect of $\epsilon, \Delta h$, and ψ_w on receptivity*

The influences of acoustic forcing level, ϵ, roughness height, Δh, and roughness obliqueness, ψ_w, were examined by conducting measurements with the matrix arrangement shown in table 2 and using samples 1–3 and 10–12 of table 1. At the location of Branch I (see table 3), the largest roughness height, Δh_3, normalized by δ^* was 0.05 and the corresponding roughness Reynolds number was $Re_{\Delta h_3} = 47$. Therefore, all roughness heights considered were well within the roughness Reynolds number range of a *hydraulically smooth* surface (see White (1974, pp. 436–439). Measurements were obtained over a range of Reynolds numbers, $R > 570$ ($x > 50.8$ cm), that extended beyond the location of Branch II (where $R = Re_{x_v}^{1/2}$). The results to be presented here were obtained for the condition where the wavelength of the wall

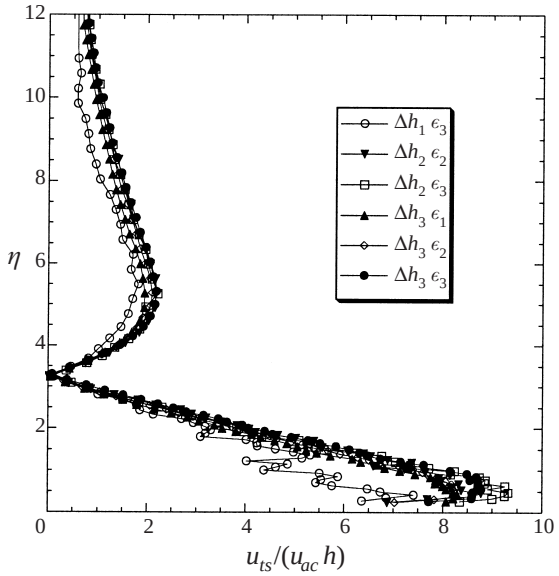

FIGURE 7. Normalized T–S amplitude profiles with two-dimensional surface waviness for various values of ϵ and Δh at $R = 1038$ ($x = 152.4$ cm), $\psi_w = 0$.

roughness λ_w matched that of the T–S wave at Branch I, the *near-resonance* condition. In this context, the term near-resonance describes the condition when $\alpha_w = \alpha_{ts,I}$ which does not account for the finite speed of the free-stream acoustic wave, i.e. $\alpha_{ac} \neq 0$.

Measurements of T–S amplitudes at locations just downstream of Branch I indicated a virtually linear response of u_{ts} with both u_{ac} and Δh in the presence of two-dimensional roughness. T–S amplitude eigenfunctions are shown in figure 7 at $R = 1038$ for various forcing products, $\epsilon\Delta h$. The r.m.s. T–S amplitude, u_{ts}, was normalized by u_{ac} and h where h is the step height normalized by the smallest step height (i.e. $h = \Delta h_n/\Delta h_1$ where $n = 1, 2$ or 3). The linear behaviour is evident from the data collapse in the figure and indicates linear receptivity for all acoustic and wall forcing levels considered. The 180° phase shift at $\eta \approx 2\delta^*$ is evident in the plots of the T–S phase ϕ_{ts} (not shown). Measured data depicting the streamwise evolution of the T–S eigenfunctions indicate good agreement with LST for locations upstream of where nonlinear effects first became apparent in the near-wall region. The nonlinear effects became evident at the same x location for a given value of $\epsilon\Delta h$, independent of the individual values of ϵ or Δh. The nonlinear evolution of the T–S instability is discussed further later.

To investigate the influence of wave obliqueness on receptivity, samples 2 and 10–12 (refer to table 1) were used to generate the oblique T–S waves by the application of oblique waviness. The roughness wavenumbers were selected to create a near-resonance condition at Branch I for each ψ_w considered (see table 3 for tabulated values of the streamwise T–S wavelength at Branch I, $\lambda_{ts,I,x}$ ($= 2\pi/\alpha_{ts,I}$)). Measured and LST T–S amplitudes at $R = 1038$ ($x = 152.4$ cm) are presented in figure 8 for various ψ_w. The LST results were normalized to match the experimental amplitudes at the maximum of u_{ts} for these profiles. Note that the relative peak (inner and outer) amplitudes of the measured T–S profiles do not scale directly with LST results. This may be due in part to non-parallel effects not accounted for in LST since non-parallelism becomes more important for three-dimensional disturbances (Bertolotti

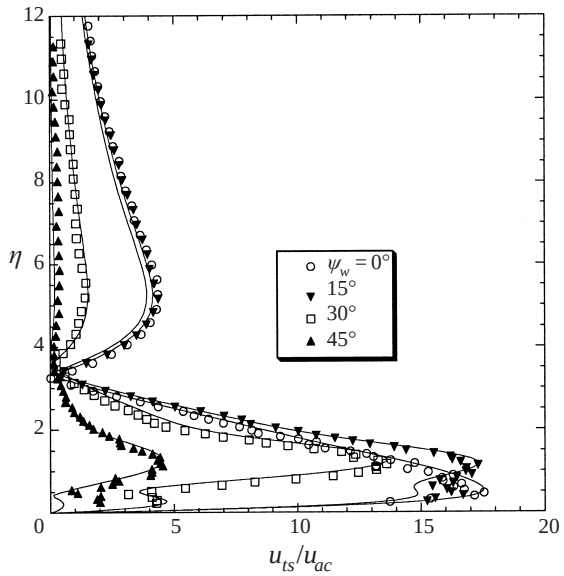

FIGURE 8. T–S amplitude profiles for various values of ψ_w at $R = 1038$ ($x = 152.4$ cm) and with forcing $(\epsilon_2, \Delta h_2)$. Symbols denote experimental data and lines LST results.

1991). Nevertheless, the salient features of the eigenfunction profiles were captured by LST. For two-dimensional disturbances, a single peak in the near-wall region below the critical layer ($\eta \approx 1$) was evident. As the disturbances became oblique, some residual of this peak remained and the appearance of a dual peak structure in the near-wall region – which straddles the critical layer – is evident. An upward shift of the global maximum to a wall-normal location above the critical layer was observed. The amplitude of the apparent residual peak reduced with increased obliqueness. An upward shift of the wall-normal location of the 180° phase jump was also evident.

The streamwise amplitude distribution of the measured T–S eigenfunctions was compared to the amplification predicted by LST. Figure 9 shows a plot of N-factor from LST versus Reynolds number along with the experimentally measured maximum T–S amplitudes. The experimental amplitudes ($\ln [u_{ts}/u_{ac}]$) were obtained from measured eigenfunction profiles taken at selected x locations and scaled for comparison with LST. Excellent agreement between the measured and LST data for two-dimensional waviness is evident except for the large values of u_{ts} measured for $R = 717$ just downstream of Branch I (in a region over the wavy surface). The large values of u_{ts} measured in the near-wall region just downstream of Branch I may partly be explained by the non-monotonic increase of the total instability response resulting from the localized peak (overshoot) in the receptivity region due to the external forcing (Crouch 1992; Choudhari 1993). The location of Branch II is in excellent agreement with LST. The data also demonstrate (not shown) that consistent amplification curves are obtainable by tracking either the inner or outer peaks, provided the response is linear. Excellent agreement was also observed between the measured and LST amplification curves for small oblique angles. The agreement became less attractive for the larger oblique angles, particularly near the location of Branch II. Again, this may be a result of non-parallel effects not captured by LST. Agreement between the measured and experimental amplifications is important since

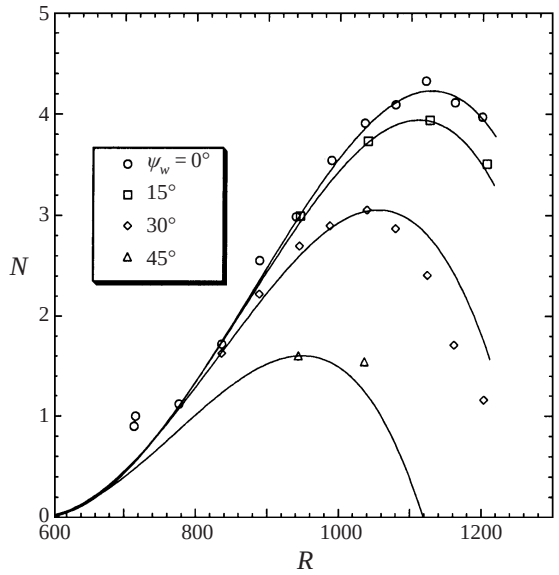

FIGURE 9. Streamwise amplification data for various values of ψ_w with forcing $(\epsilon_2, \Delta h_2)$: symbols, experimental measurements; lines, LST.

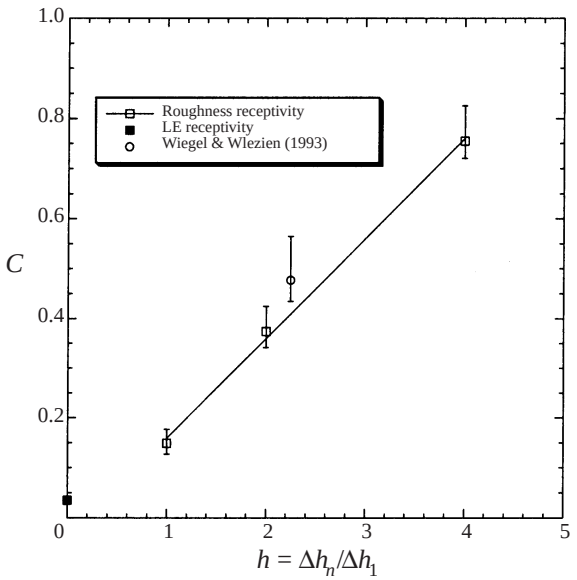

FIGURE 10. Non-localized two-dimensional receptivity coefficients from the present experiment ($F = 55 \times 10^{-6}$) and a past experiment ($F \approx 46 \times 10^{-6}$) as a function of Δh.

theory (e.g. LST) is required to backtrack the effective Branch I amplitudes in an accurate fashion.

The receptivity coefficients, C, to be presented were referenced to Branch I and computed utilizing (2.2). It was stipulated that all values of u_{ts} employed be obtained downstream of Branch I and the roughness surface and upstream of Branch II. Figure 10 shows a plot of the experimental two-dimensional receptivity coefficients

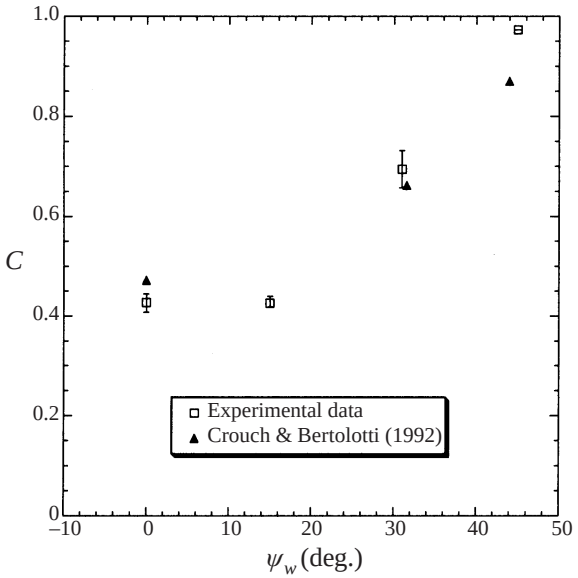

FIGURE 11. Measured ($F = 55 \times 10^{-6}$) and theoretical ($F = 56 \times 10^{-6}$) receptivity coefficients versus ψ_w with forcing ($\epsilon_2 \Delta h_2$).

(plus linear regression fit) versus the normalized step height. Data from the experiment of Wiegel & Wlezien (1993) for a different non-dimensional frequency ($F \approx 46 \times 10^{-6}$) are also included. The symbols represent mean values and the error bars the maximum plus/minus deviations observed in the measurements for all values of ϵ. The leading-edge receptivity coefficient for the smooth surface ($h = 0$) was calculated using data obtained in short streamwise surveys. The small values of the leading-edge receptivity coefficients ($C \approx 0.035$) support the decomposition assumption discussed previously. Saric *et al.* (1995) obtained leading-edge coefficients at $F = 55 \times 10^{-6}$ of $C \approx 0.030$ and $C \approx 0.048$ with a 20 : 1 and 40 : 1 modified super ellipse, respectively. Good agreement is observed between the present and previous (Wiegel & Wlezien 1993) experimental receptivity coefficients. The corresponding T–S wave kinematics were inferred from data obtained with short streamwise surveys (i.e. ϕ_{ts} versus x data) where $\alpha_{ts}(= -\mathrm{d}\phi_{ts}/\mathrm{d}x)$ was computed directly. The average T–S wave phase speed, $\bar{c}_{ph}/U_\infty = 0.33$ ($c_{ph} = 2\pi f_o/\alpha_{ts}$), at $R = 1038$ for all values of ϵ and Δh considered is in excellent agreement with the LST result, $c_{ph}/U_\infty = 0.33$.

Figure 11 shows a plot of measured receptivity coefficients as a function of ψ_w along with theoretical data ($F = 56 \times 10^{-6}$) by Crouch & Bertolotti (1992). The agreement between the measured and theoretical data is good, thereby providing experimental evidence of increased receptivity with increased wave obliqueness. The confidence level for the value of the experimental receptivity coefficient at $\psi_w = 45^\circ$ is not very high since only one data point was used to obtain the value of C. This may be one explanation for the large difference observed there along with the fact that the mode-interaction theory used to compute the theoretical values of C degrades with three-dimensionality, which is largely attributable to non-parallel effects as noted by Crouch & Bertolotti (1992). The overall agreement between the measured and LST c_{ph}/U_∞ with respect to ψ_w is good, within the experimental uncertainty of the measurements.

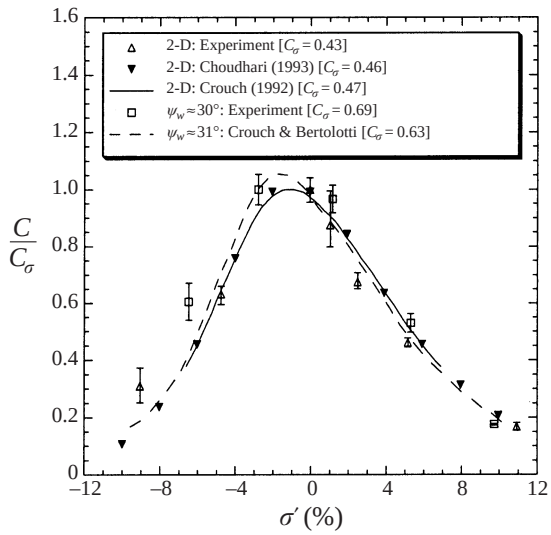

FIGURE 12. Measured ($F = 55 \times 10^{-6}$) and theoretical ($F = 55 \times 10^{-6}$ and $F = 56 \times 10^{-6}$) receptivity coefficients versus the detuning parameter with forcing ($\epsilon_2, \Delta h_2$).

3.2.2. *Effect of detuning on receptivity*

In this section, results are presented for the so-called *detuned* conditions. Detuning is referred to as the condition when there is a mismatch between the wavelengths of the wall roughness and the T–S mode ($\lambda_w \neq \lambda_{ts}$) for a given disturbance frequency. The energy transfer from the forced disturbance becomes less efficient as the degree of detuning is increased. As a measure of the detuning, the detuning parameter σ is defined as

$$\sigma = \frac{\alpha_w - \alpha_{ts,I}}{\alpha_{ts,I}}. \tag{3.1}$$

In previous studies (e.g. Wiegel & Wlezien 1993), detuning was generally examined by varying U_∞, which consequently varied $\alpha_{ts,I}$. This was done because of difficulties in varying α_w. Because of the type of receptivity sites used in the current study, σ was varied by changing α_w. Detuning data for both two-dimensional and oblique waviness were obtained using samples 2 and 4–9 and samples 11 and 13–16, respectively (refer to table 1). All the data were obtained with the forcing product $\epsilon_2 \Delta h_2$.

The maximum receptivity was not expected at the near-resonance condition $\alpha_w = \alpha_{ts,I}$ as predicted by receptivity theory that assumes incompressible flow (infinite acoustic wave speed). To account for a finite acoustic wave speed, one has to take into consideration the wavenumber of the free-stream acoustic wave, α_{ac}, as conjectured by Wiegel & Wlezien (1993). For the present experiment, care was taken to acoustically excite the free-stream with a downstream-travelling wave. Choudhari & Streett (1994) discussed the finite wave speed effect and showed that a resonance condition exists when $(\alpha_w, \beta_w) = (\alpha_{ts,I} - \alpha_{ac}, \beta_{ts,I})$ since $\beta_{ac} = 0$ here.

Measured and theoretical (Choudhari 1993; Crouch 1992; Crouch & Bertolotti 1992) receptivity coefficients are presented in figure 12 for various values of the detuning parameter (modified) σ'. The roughness height used to compute the theoretical receptivity coefficients for single-mode waviness was the first Fourier coefficient of a square wave pattern with height Δh, namely the mode corresponding to the fundamental wavenumber, α_w, with amplitude $\Delta h/\pi$. The parameter σ' shifts the

values of σ in (3.1) to account for the finite acoustic wave speed. The detuning parameters are related by $\sigma' = \sigma + \alpha_{ac}/\alpha_{ts,I}$ where the respective values of $\alpha_{ac}/\alpha_{ts,I}$ for the two-dimensional and oblique waviness are 1.04% and 1.08%. The receptivity coefficients are normalized by C_σ where C_σ is the maximum value of C (measured or computed) except for the theoretical C_σ value for the oblique roughness which is the theoretical value of C at the same $\sigma'(\approx -2.8)$ as the corresponding experimental value. Good agreement is obtained between the measured and theoretical receptivity coefficients over a wide range of α_w. A maximum difference of less than 10% was obtained between the measured maximum and the corresponding theoretical value of the receptivity coefficients, C_σ. The decrease in the receptivity with increased detuning suggests that the receptivity produced by naturally occurring surface roughness may be much smaller than the values measured here for an equivalent r.m.s. roughness height.

3.3. *Disturbance evolution*

In this section, data describing the evolution of the boundary-layer disturbance field are presented. A number of experimental investigations has been conducted in the past to study this phenomenon, most of which were primarily concerned with instabilities generated within the boundary layer (e.g. vibrating ribbons, periodic surface blowing/suction, etc.). However, the present work focuses on externally (at least partially) generated instabilities where the temporal and spatial scales are completely decoupled. Emphasis is placed on results obtained in the presence of two-dimensional surface roughness since nonlinear behaviour was evident only for large values of the forcing combination ($\epsilon\Delta h$). The broadband results obtained with oblique waviness were qualitatively similar to those obtained with two-dimensional waviness and intermediate forcing, $\epsilon_2\Delta h_2$. For this reason, oblique results are not discussed explicitly in this section except where minor differences were noted. The measured streamwise amplitude distribution of the normalized T–S eigenfunctions are compared for various values of $\epsilon\Delta h$ in figure 13. The solid symbols represent data for the outer peak and the open symbols data for the inner (maximum) peak. Nonlinear effects are evident from the amplification curves for the forcing products of $\epsilon_2\Delta h_3$ and $\epsilon_3\Delta h_3$ (see for comparison figure 9). For the case of $\epsilon_2\Delta h_3$, nonlinear effects are apparent only in the near-wall region and first become discernible when $u_{ts}/U_\infty > 0.8\%$ at $R \approx 1120$ (just upstream of Branch II, $R_{II} = 1129$). For the largest forcing product ($\epsilon_3\Delta h_3$), nonlinearity is evident in both the near-wall and outer regions of the boundary layer. The nonlinearity was observed first near the surface and eventually spread throughout the shear layer due to the interaction of normal vorticity, which is driven by the mean shear (see Cohen, Breuer & Haritonidis 1991). Nonlinearity was first observed for $u_{ts}/U_\infty > 1.0\%$ at $R \approx 1034$ ($R < R_{II}$).

Broadband ($2 < f < 400$ Hz) r.m.s. fluctuating velocities, u, measured for $\epsilon_2\Delta h_2$ are presented in figure 14. For this intermediate forcing level, the flow remained laminar (see figure 13). In the early stages ($R < 943$, $x < 127$ cm), the r.m.s. velocity profiles resemble those of Klebanoff modes as measured by Klebanoff (1971), and Kendall (1985, 1990). The profiles are indistinguishable from profiles measured on the smooth model surface with no controlled acoustic forcing (baseline configuration): $\epsilon = 0$, $\Delta h = 0$. The maximum r.m.s. fluctuations occur near the midpoint of the boundary-layer thickness ($\eta \sim 2.3$) and are three orders of magnitude less than U_∞. The rate of increase of the maximum r.m.s. velocity at each streamwise station is small for these low-free-stream turbulence intensity levels. For measurements taken further downstream ($R > 943$), the contributions from the T–S wave become dominant in

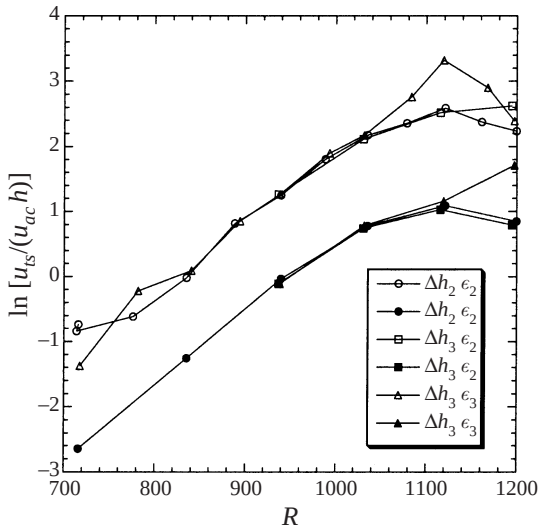

FIGURE 13. Streamwise amplification data with two-dimensional disturbances for various values of $\epsilon\Delta h$ at $\psi_w = 0$. Open symbols, inner peaks; solid symbols, outer peaks.

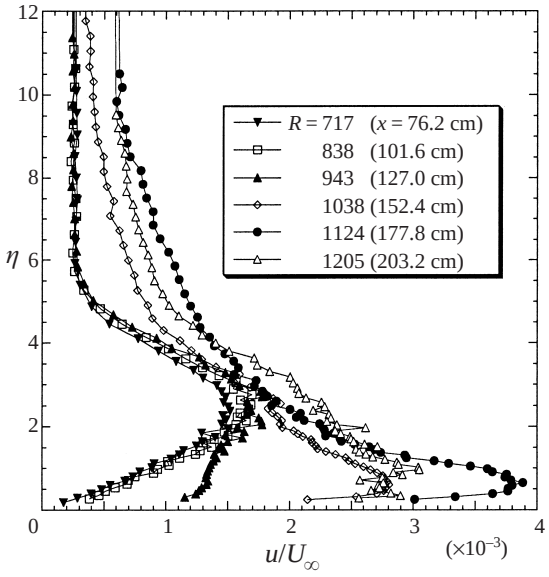

FIGURE 14. Measured broadband r.m.s. fluctuating velocity for forcing combination of $\epsilon_2\Delta h_2$.

the near-wall region and near the boundary-layer edge due to the dual-lobe shape of the T–S eigenfunctions. Near the midpoint of the boundary layer, the r.m.s. velocities are still consistent with those measured on the baseline configuration. As shown using parabolized stability theory by Herbert & Lin (1993), the T–S waves and these low-frequency Klebanoff modes appear to exist independently, but both may contribute to the intensity at a given frequency. For $\epsilon_3\Delta h_3$ where nonlinear effects and consequent breakdown occurred, increases of one to two orders of magnitude in the maximum values of u were observed. Power spectral densities of the fluctuating streamwise velocity, PSD_u, corresponding to data presented in figure 14 are shown in

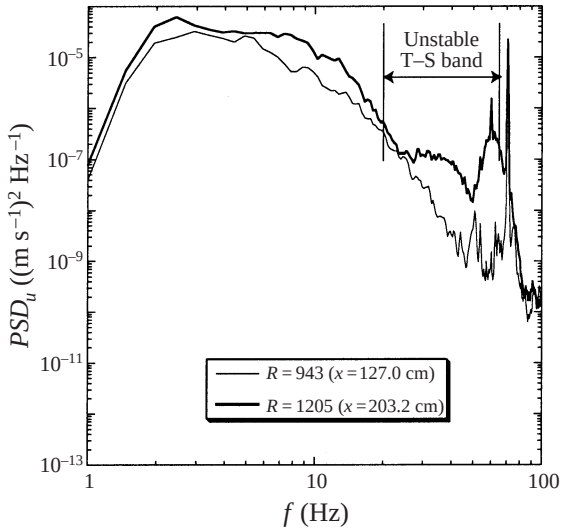

FIGURE 15. Spectra of fluctuating velocity near $\eta \approx 2.3$ for forcing product of $\epsilon_2 \Delta h_2$.

figure 15. The spectra are shown for data obtained at $\eta \approx 2.3$. The controlled acoustic forcing is clearly evident in the spectra at $f_o = 71$ Hz. The spectra shown consist of significant low-frequency energy, a characteristic of Klebanoff modes. Modest amplification at frequencies ($f < 20$ Hz) below the unstable T–S modes is evident at $R = 1205$ ($x = 203.2$ cm) and was also observed for the baseline configuration. As expected, significantly more amplification is evident in the unstable T–S band.

To investigate the coherent nature of the boundary-layer disturbance field, particular consideration was given to disturbances at the fundamental (f_o), subharmonic ($f_o/2$), and first harmonic ($2f_o$) frequencies. The coherence function, γ, (between the designated instability wave and the input signal used for the acoustic forcing) at the three frequencies of interest was computed. Significant values of γ for $\epsilon_2 \Delta h_2$ were obtained at the fundamental and harmonic frequencies for a wall-normal location corresponding to the maximum of the T–S wave amplitude; however, negligible coherence was observed for the subharmonic band. The amplification curves at both the fundamental and harmonic frequencies reveal growth, even for the small harmonic amplitudes measured, with subsequent amplitude decay. The growth rate of the harmonic disturbance is approximately twice that of the fundamental for this weak nonlinear interaction. No amplification was observed at the subharmonic frequency. Coherence and amplification data for $\epsilon_3 \Delta h_3$ are shown in figure 16. A sharp roll off in coherence of the fundamental and harmonic disturbances is evident for $R > 1038$ ($x > 152.4$ cm) indicating the onset of significantly nonlinear behaviour leading to turbulence. This is in agreement with results inferred from the amplification curves in figure 13. Again, negligible coherence was observed at the subharmonic frequency. Referring to figure 16(b), it is evident from the amplification curves that the harmonic disturbance grew at a rate different (i.e. twice) from that of the fundamental, indicating a strong nonlinear interaction at the harmonic frequency. The growth seen at the subharmonic frequency was not due to phase-locked amplification, but a result of broadening of the spectra indicative of the breakdown process. The transition Reynolds number for this scenario was $Re_{tr} \approx 1.2 \times 10^6$ which is approximately one-third of the baseline $Re_{tr} (\approx 3.2 \times 10^6)$.

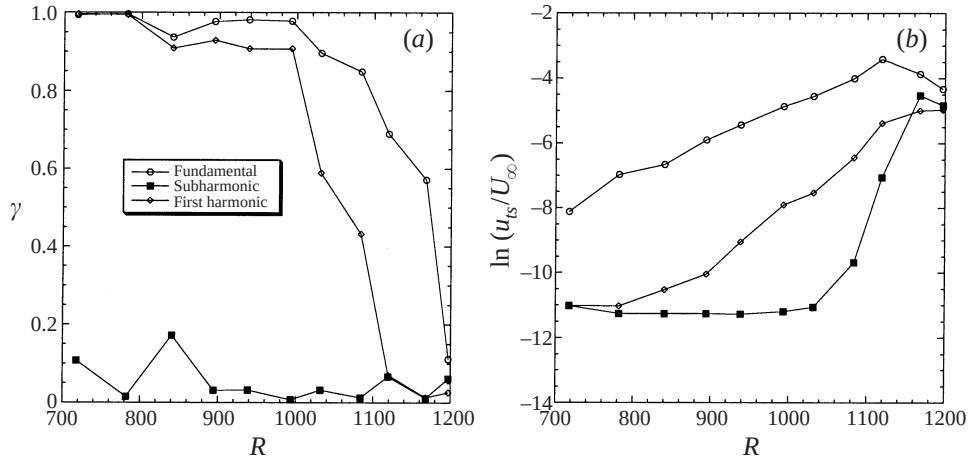

FIGURE 16. Data showing the fundamental, subharmonic, and first harmonic (*a*) coherence functions and (*b*) growth curves for $\epsilon_3 \Delta h_3$.

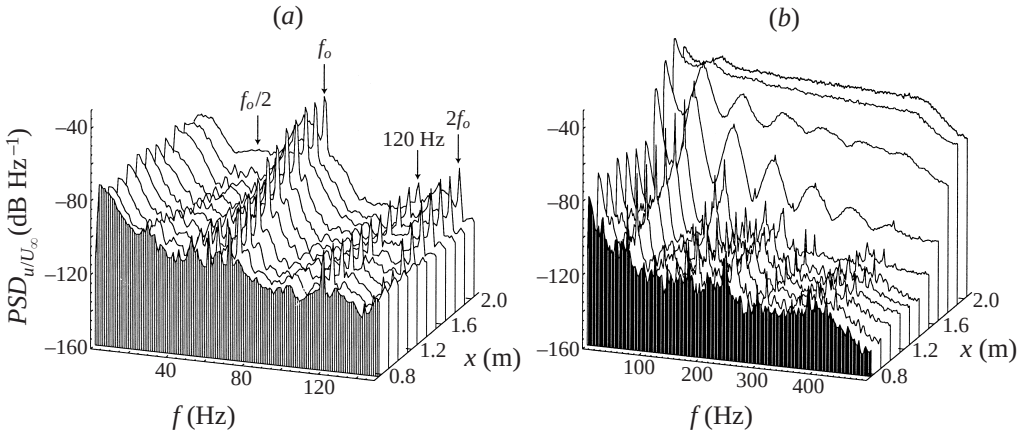

FIGURE 17. Spectra of streamwise velocity taken at $u_{ts,max}$ over a range of streamwise locations for (*a*) $\epsilon_2 \Delta h_2$ and (*b*) $\epsilon_3 \Delta h_3$. The subharmonic, fundamental, and first harmonic frequencies (along with 120 Hz electronic noise) are denoted in (*a*).

Finally, broadband spectra for the intermediate and largest forcing levels are presented in figure 17 for a range of streamwise locations ($717 < R < 1205$ or $76.2 < x < 203.2$ cm) at wall-normal locations corresponding to the maximum of u_{ts}. For the intermediate forcing level ($\epsilon_2 \Delta h_2$) in figure 17(*a*), the energy and associated growth at the fundamental forcing frequency ($f_o = 71$ Hz) and its first harmonic are clearly evident. The energy at $f = 120$ Hz is associated with electronic noise as is evident from the constant streamwise amplitude. Amplification of broadband energy centred about $f \approx 60$ Hz, presumably a result of the *natural* tunnel disturbance environment, is discernible in the spectra for $x > 127.0$ cm ($R > 943$). Broadband amplification is also evident about $f \approx 130$ Hz for $x > 152.4$ cm ($R > 1038$). This latter broadband energy is possibly an interaction between the forced T–S wave and the naturally occurring broadband T–S field. The broadband amplification about $f \approx 130$ Hz was not evident for the oblique waviness configuration ($\psi_w = 30°$). This is believed to be due to the reduced energy amplitudes of both the forced T–S wave

and the naturally occurring broadband T–S field. The situation was quite different for the largest forcing combination in figure 17(*b*). The presence of significant energy at the fundamental and higher harmonic frequencies is clearly discernible at the onset of nonlinearity ($x > 152.4$ cm or $R > 1038$). The harmonic bands broaden until a developed turbulent spectrum was obtained. Broadband amplification in the unstable T–S band of frequencies as seen for the intermediate forcing level above was not discernible in the present spectra. Similar harmonic-dominated spectra were obtained in the experiment of Breuer *et al.* (1996). This type of breakdown from laminar to turbulent flow as obtained by the classical results of Klebanoff & Tidstrom (1959) and Klebanoff, Tidstrom & Sargent (1962) is indicative of a K-type breakdown believed to derive from primary resonance (Herbert 1985). The selectivity of the single-frequency wave, imposed by the controlled acoustic forcing and receptivity sites, created a dominant primary T–S wave with amplitudes much larger than other two- and three-dimensional modes resulting from background disturbances. The primary mode at the fundamental frequency dominated the breakdown process, and resulting nonlinear interactions produced harmonics as is evident in the disturbance spectral evolution (see figure 17*b*).

4. Concluding remarks

The objective of the current research was to better understand the acoustic receptivity process and subsequent disturbance evolution in the presence of wavy surfaces and correlate results with theory. Experimental investigations were conducted to examine acoustic receptivity and subsequent boundary-layer instability evolution in the presence of two-dimensional and oblique surface waviness. These investigations provided a data base which can ultimately be used to validate current and future theoretical receptivity/transition models needed to improve the current understanding of laminar-to-turbulent transition.

A subtle accomplishment of the current study was the ability to introduce a variety of steady boundary-layer disturbances via the well-defined receptivity sites without any measurable first-order effects on the base flow. This study explored, in addition to two-dimensional acoustic receptivity, the subsequent evolution of the boundary-layer instability. The current acoustic receptivity measurements with two-dimensional waviness are in excellent agreement with the existing experimental measurements of Wiegel & Wlezien (1993) and theoretical results of Crouch (1992) and Choudhari (1993). For a configuration where laminar-to-turbulent breakdown occurred ($\epsilon_3 \Delta h_3$), the breakdown process was found to be dominated by energy at the fundamental and higher-harmonic frequencies, indicative of K-type breakdown. Receptivity data were acquired experimentally for the first time over oblique wavy surfaces ($\psi_w = 15°, 30°$, and $45°$) to measure the dependence of receptivity on roughness obliqueness (or three-dimensionality). The current findings were in substantial agreement with theory and experimentally confirmed the earlier theoretical results by Crouch & Bertolotti (1992) that receptivity increases markedly with wave obliqueness. Boundary-layer transition was not observed for the forcing combination ($\epsilon_2 \Delta h_2$) used with the oblique surface waviness.

The transition Reynolds number measured on the baseline configuration was $Re_{tr} \approx 3.2 \times 10^6$. The value of Re_{tr} for the two-dimensional surface roughness with a forcing combination of $\epsilon_3 \Delta h_3$ was significantly less ($\sim 60\%$ reduction) than that for the baseline configuration. The drastic shifts in the value of Re_{tr} demonstrate

the sensitivity of the transition location to the free-stream environment and surface conditions.

This paper was presented at the AIAA Fluids 2000 Conference in Denver, Colorado on 19–22 June 2000.

REFERENCES

Aizin, L. B. & Polyakov, N. F. 1979 Acoustic generation of Tollmien–Schlichting waves over local unevenness of surface immersed in streams. *Preprint 17, Akad. Nauk USSR, Siberian Div., Inst. Theor. Appl. Mech., Novorsibirsk* (in Russian).

Bertolotti, F. P. 1991 Linear and nonlinear stability of boundary layers with streamwise varying properties. PhD thesis, The Ohio State University, Columbus, OH.

Breuer, K. S., Dzenitis, E. G., Gunnarsson, J. & Ullmar, M. 1996 Linear and nonlinear evolution of boundary layer instabilities generated by acoustic-receptivity mechanisms. *Phys. Fluids* **8**, 1415–1423.

Choudhari, M. 1993 Boundary-layer receptivity due to distributed surface imperfections of a deterministic or random nature. *Theor. Comput. Fluid Dyn.* **4**, 101–117.

Choudhari, M. & Streett, C. L. 1994 Theoretical prediction of boundary-layer receptivity. *AIAA Paper* 94–2223.

Cohen, J., Breuer, K. S. & Haritonidis, J. H. 1991 On the evolution of a wave packet in a laminar boundary layer. *J. Fluid Mech.* **225**, 575–606.

Crouch, J. D. 1991 Initiation of boundary-layer disturbances by nonlinear mode interactions. In *Boundary Layer Stability and Transition to Turbulence* (ed. D. C. Reda, H. L. Reed & R. Kobayashi). ASME, vol. 114, pp. 63–68.

Crouch, J. D. 1992 Non-localized receptivity of boundary layers. *J. Fluid Mech.* **244**, 567–581.

Crouch, J. D. & Bertolotti, F. P. 1992 Nonlocalized receptivity of boundary layers to three-dimensional disturbances. *AIAA Paper* 92–0740.

Goldstein, M. E. 1983 The evolution of Tollmien–Schlichting waves near a leading edge. *J. Fluid Mech.* **127**, 59–81.

Goldstein, M. E. 1985 Scattering of acoustic waves into Tollmien–Schlichting waves by small streamwise variations in surface geometry. *J. Fluid Mech.* **154**, 509–529.

Goldstein, M. E., Sockol, P. M. & Sanz, J. 1983 The evolution of Tollmien–Schlichting waves near a leading edge. Part 2. Numerical determination of amplitudes. *J. Fluid Mech.* **129**, 443–453.

Herbert, T. 1985 Three-dimensional phenomena in the transitional flat-plate boundary layer. *AIAA Paper* 85–0489.

Herbert, T. & Lin, N. 1993 Studies of boundary-layer receptivity with parabolized stability equations. *AIAA Paper* 93–3053.

Kendall, J. M. 1985 Experimental study of disturbances produced in a pre-transitional laminar boundary layer by weak freestream turbulence. *AIAA Paper* 85–1695.

Kendall, J. M. 1990 Boundary layer receptivity to freestream turbulence. *AIAA Paper* 90–1504.

King, R. A. 2000 Receptivity and growth of two- and three-dimensional disturbances in a Blasius boundary layer. PhD thesis, Massachusetts Institute of Technology, Cambridge, MA.

Klebanoff, P. S. 1971 Effect of freestream turbulence on the laminar boundary layer. *Bull. Am. Phys. Soc.* **10** (11), 1323.

Klebanoff, P. S. & Tidstrom, K. D. 1959 Evolution of amplified waves leading to transition in a boundary layer with zero pressure gradient. *NASA TN* D-195.

Klebanoff, P. S., Tidstrom, K. D. & Sargent, L. M. 1962 The three-dimensional nature of boundary-layer instability. *J. Fluid Mech.* **12**, 1–34.

Kobayashi, R., Fukunishi, Y. & Kato, T. 1996 Laminar flow control of boundary layers utilizing acoustic receptivity. In *Sixth Asian Congress of Fluid Mechanics* (ed. Y. T. Chew & C. P. Tso), pp. 629–632. Centre for Continuing Education, Nanyang Technological University.

Kobayashi, R., Fukunishi, Y., Nishikawa, T. & Kato, T. 1995 The receptivity of flat-plate boundary-layers with two-dimensional roughness elements to freestream sound and its control. In *Laminar-Turbulent Transition* (ed. R. Kobayashi). IUTAM, vol. IV, pp. 507–514. Springer.

Kosorygin, V. S., Radeztsky, R. H. & Saric, W. S. 1995 Laminar boundary-layer, sound receptivity

and control. In *Laminar–Turbulent Transition* (ed. R. Kobayashi). IUTAM, vol. IV, pp. 517–524. Springer.

Malik, M. R. 1992 e^{Malik}: A new spatial stability analysis program for transition prediction using the e^N method. *High Technology Rep.* HTC-9203, Hampton, Virginia.

Morkovin, M. V. 1969 Critical evaluation of transition from laminar to turbulent shear layers with emphasis on hypersonically traveling bodies. *Tech. Rep.* AFFDL-TR-68-149. Wright–Patterson Air Force Base.

Nishioka, M. & Morkovin, M. V. 1986 Boundary-layer receptivity to unsteady pressure gradients: experiments and overview. *J. Fluid Mech.* **171**, 219–261.

Ruban, A. I. 1985 On the generation on Tollmien–Schlichting waves by sound. *Fluid Dyn.* **19**, 709–716.

Saric, W. S. 1994 Low-speed boundary-layer transition experiments. In *Transition: Experiments, Theory & Computations* (ed. T. C. Corke, G. Erlebacher & M. Y. Hussaini), pp. 1–114. Oxford.

Saric, W. S., Hoos, J. A. & Kohama, Y. 1990 Boundary-layer receptivity: Part 1. Freestream sound and 2D roughness strips. *CEAS-CR-R*-90191. College of Engineering and Applied Sciences Report, Arizona State University.

Saric, W. S., Hoos, J. A. & Radeztsky, R. H. 1991 Boundary-layer receptivity of sound with roughness. In *Boundary Layer Stability and Transition to Turbulence* (ed. D. C. Reda, H. L. Reed & R. Kobayashi). ASME, vol. 114, pp. 17–22.

Saric, W. S. & White, E. B. 1998 Influence of high-amplitude noise on boundary-layer transition to turbulence. *AIAA Paper* 98–2645.

Saric, W. S., Wie, W., Rasmussen, B. K. & Krutckoff, T. K. 1995 Experiments on leading-edge receptivity to sound. *AIAA Paper* 95-2253.

White, F. M. 1974 *Viscous Fluid Flow*. McGraw-Hill.

Wiegel, M. & Wlezien, R. W. 1993 Acoustic receptivity of laminar boundary layers over wavy walls. *AIAA Paper* 93-3280.

Wlezien, R. W. 1994 Measurement of acoustic receptivity. *AIAA Paper* 94-2221.

Wlezien, R. W., Parekh, D. E. & Island, T. C. 1990 Measurement of acoustic receptivity at leading edges and porous strips. *Appl. Mech. Rev.* **43**(5), S167–S174.

Zavol'skii, N. A., Reutov, V. P. & Rybushkina, G. V. 1984 Excitation of Tollmien–Schlichting waves by acoustic and vortex disturbance scattering in boundary layer on a wavy surface. *J. Appl. Mech. Tech. Phys.* **25**, 355–361, (English translation, 1983).

Zhou, M. D., Liu, D. P. & Blackwelder, R. F. 1994 An experimental study of receptivity of acoustic waves in laminar boundary layers. *Exps. Fluids* **17**, 1–9.